Navier-Stokes Solutions About the F/A-18 Forebody-Leading-Edge Extension Configuration

Farhad Ghaffari,* James M. Luckring,† and James L. Thomas‡
NASA Langley Research Center, Hampton, Virginia
and
Brent L. Bates§
Vigyan, Inc., Hampton, Virginia

Three-dimensional viscous flow computations are presented for the F/A-18 forebody including the leading-edge extension geometry. Solutions are obtained from an algorithm for the compressible Navier-Stokes equations that incorporates an upwind-biased, flux-difference-splitting approach along with longitudinally patched grids. Results are presented for both laminar and fully turbulent flow assumptions and include correlations with wind-tunnel as well as flight-test results. A good quantitative agreement for the forebody surface pressure distribution is achieved between the turbulent computations and wind-tunnel measurements at $M_\infty = 0.6$. The computed turbulent surface flow patterns on the forebody qualitatively agree well with in-flight surface flow patterns obtained on an F/A-18 aircraft at $M_\infty = 0.34$.

Nomenclature

C_L = lift coefficient, $=\text{lift}/q_\infty S_{\text{ref}}$
C_p = pressure coefficient, $=(p-p_\infty)/q_\infty$
$\bar{c}$ = wing mean aerodynamic chord, 8.294 in.
c_p = specific heat at constant pressure
c_v = specific heat at constant volume
E_0 = total energy per unit volume
$\hat{F}, \hat{G}, \hat{H}$ = flux vectors
h_0 = total enthalpy, $=(E_0+p)/\rho$
J = Jacobian of the coordinate transformation
k = conductivity, $=c_p\mu/Pr$
M_∞ = freestream Mach number
Pr = Prandtl number
$\hat{Q}$ = state vector, $=J^{-1}[\rho,\rho u,\rho v,\rho w,E_0]^T$
q = total velocity
q_∞ = freestream dynamic pressure
$R_{\bar{c}}$ = Reynolds number based on $\bar{c}$
S_{ref} = area of reference wing planform
u,v,w = body-axis Cartesian velocity components
v^* = wall-friction velocity, $=\sqrt{\tau_w/\rho}$
$x/\bar{c}$ = normalized distance aft of nose
y/s = fraction of LEX exposed semispan
y^+ = inner-law variable, $=yv^*/v$
α = angle of attack, deg
γ = ratio of specific heats, $=c_p/c_v$
θ = azimuthal angle
μ = viscosity
ν = kinematic viscosity, $=\mu/\rho$
ξ,η,ζ = body-fitted coordinates
ρ = density
τ_w = wall shear stress

Introduction

ADVANCES in numerical solution methodology along with increased computer speed and capacity have made it feasible to seek numerical solutions to the three-dimensional Navier-Stokes equations for relatively complicated geometries. Prior computations for isolated wing[1-3] or body[4-6] geometries have demonstrated that accurate Navier-Stokes solutions are not limited to benign flow conditions; converged results can be obtained that include complex flow structures (e.g., three-dimensional separation, shocks, vortices, etc.) as well as interactions among these structures.

Applications to aircraft configurations have been less forthcoming primarily due to complexities associated with grid gen-

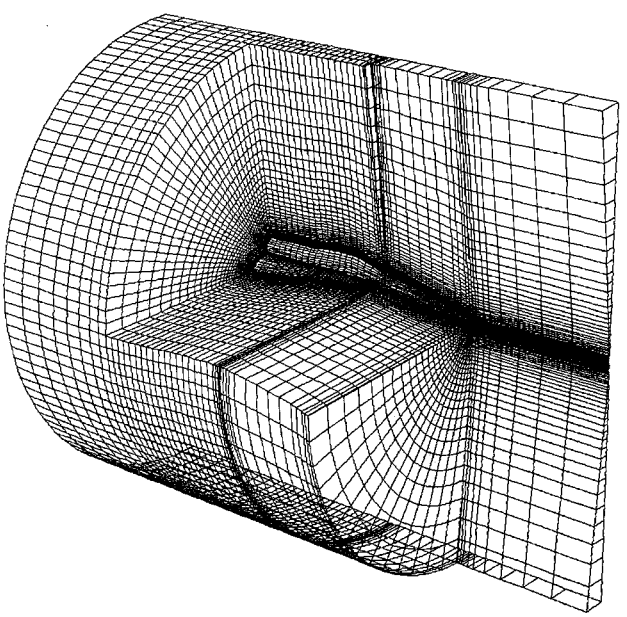

Fig. 1 Blocking strategy for the F/A-18 forebody-LEX grid.

Presented as Paper 89-0338 at the AIAA 27th Aerospace Sciences Meeting, Jan. 9-12, 1989, Reno, NV; received April 15, 1989; revision received Dec. 20, 1989; accepted for publication Feb. 11, 1990.

*Research Engineer, Transonic Aerodynamics Branch. Senior Member AIAA.
†Assistant Branch Head, Transonic Aerodynamics Branch. Associate Fellow AIAA.
‡Senior Research Scientist, Computational Methods Branch. Associate Fellow AIAA.
§Research Engineer. Member AIAA.

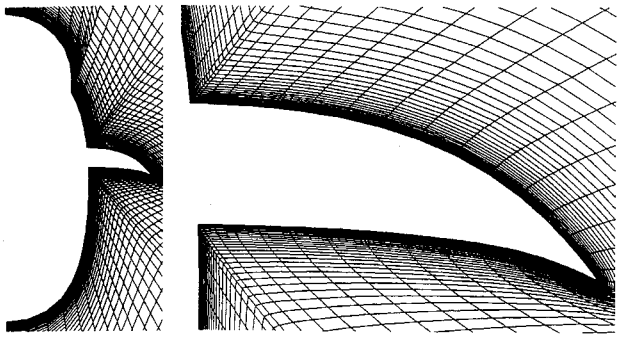

Fig. 2 F/A-18 typical crossflow and detail LEX-body grid.

eration and surface definition along with the relatively large computational resources required for these cases. Nonetheless, recent progress has been shown for several cases including supersonic inviscid flow calculations about the F/A-18 forebody-leading-edge extension (LEX) and the SR-71,[7] a complete advanced fighter-type configuration,[8] as well as the computations about the complete F-14 fighter aircraft[9] at transonic speeds. Progress has also been made in applying the thin-layer Navier-Stokes methodology to complex aircraft configurations; examples include transonic computations about the complete F-16A aircraft[10] as well as a transport wing/body configuration.[11] Most recently, viscous flow computations about the ascent configuration of the Space Shuttle[12] have demonstrated good correlation with flight data at subsonic, transonic, and supersonic speeds.

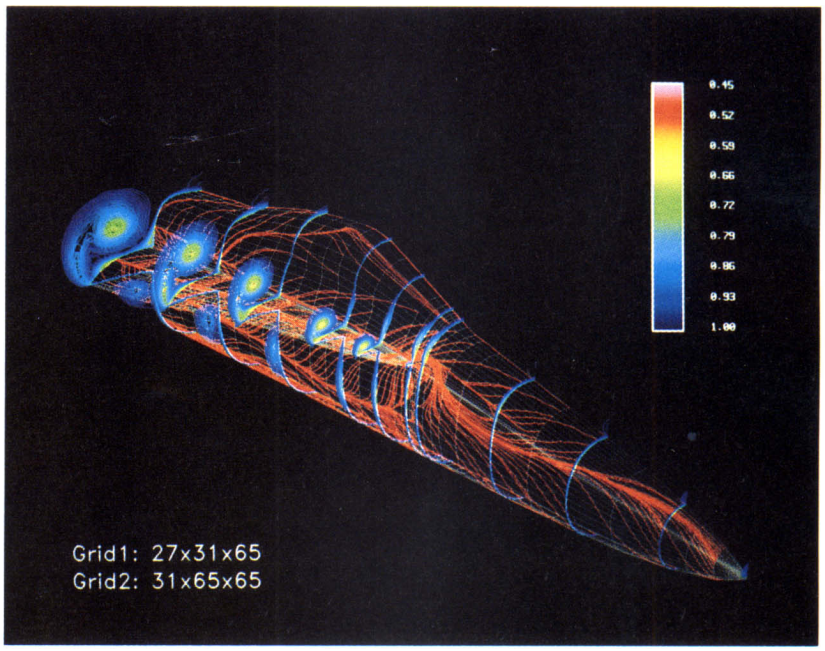

a) Laminar

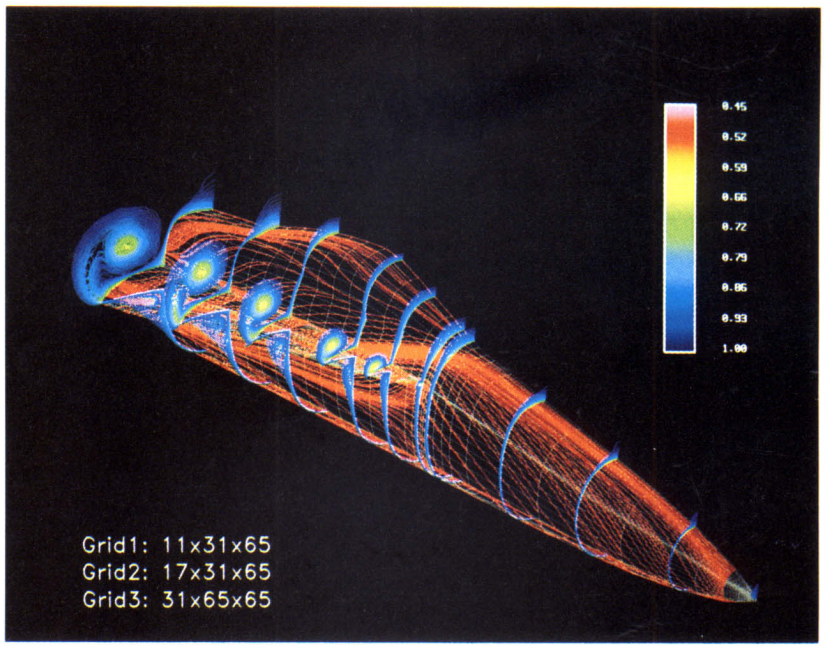

b) Turbulent

Fig. 3 Total pressure contours with surface flow pattern – overall view: $M_\infty = 0.6$, $R_{\bar{c}} = 0.8 \times 10^6$, $\alpha = 20$ deg.

The present investigation is directed toward applying an extended version of an implicit Navier-Stokes algorithim[1,3,6] to the F/A-18 forebody-LEX geometry at conditions suitable to the formation of separated subsonic and, in some cases, transonic flows. The extension to the algorithm permits longitudinally blocked grids, which is an efficient procedure, for accurately modeling the subject configuration. The F/A-18 has been selected for this study primarily due to the availability of current wind-tunnel[13] as well as flight research[14] data related to an ongoing high angle-of-attack research program being conducted by NASA.

The computations are focused on two specific flow conditions in accordance with the recent wind-tunnel and flight-test research. The wind-tunnel conditions are $M_\infty = 0.6$, $R_{\bar{c}} = 0.8 \times 10^6$, and $\alpha = 20$ deg, which correspond to recent tests conducted at the David Taylor Research Center (DTRC) 7 × 10-ft tunnel with a 6% F/A-18 model. At these conditions, the forebody flow could be transitional, hence, both laminar as well as turbulent solutions are obtained. However, only turbulent computations are performed at $M_\infty = 0.34$, $R_{\bar{c}} = 13.5 \times 10^6$, and $\alpha = 19$ deg, which correspond to recent flight tests of the NASA F/A-18 High Alpha Research Vehicle (HARV) conducted at the Dryden Flight Research Facility.

Governing Equations

The governing equations as well as computational method for the present investigation have been published many times

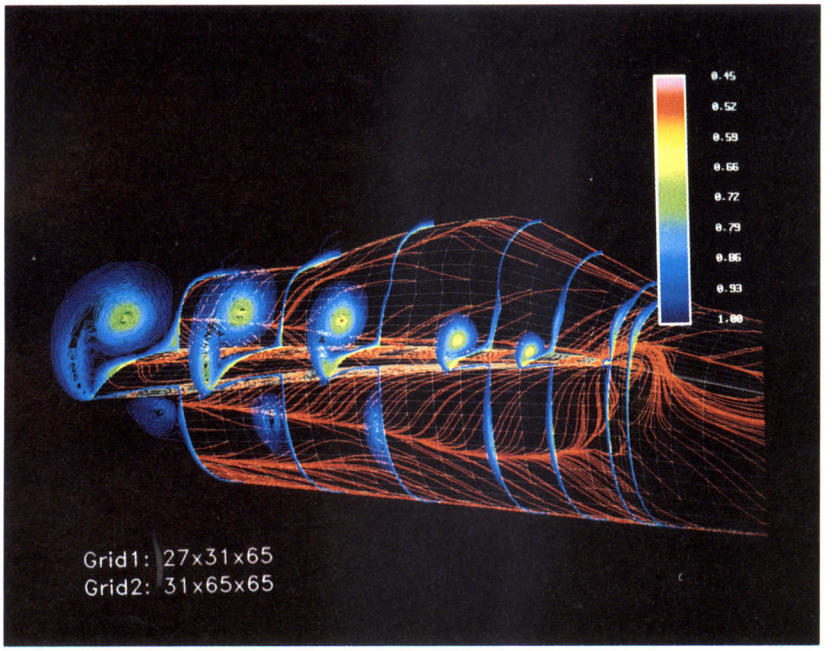

a) Laminar

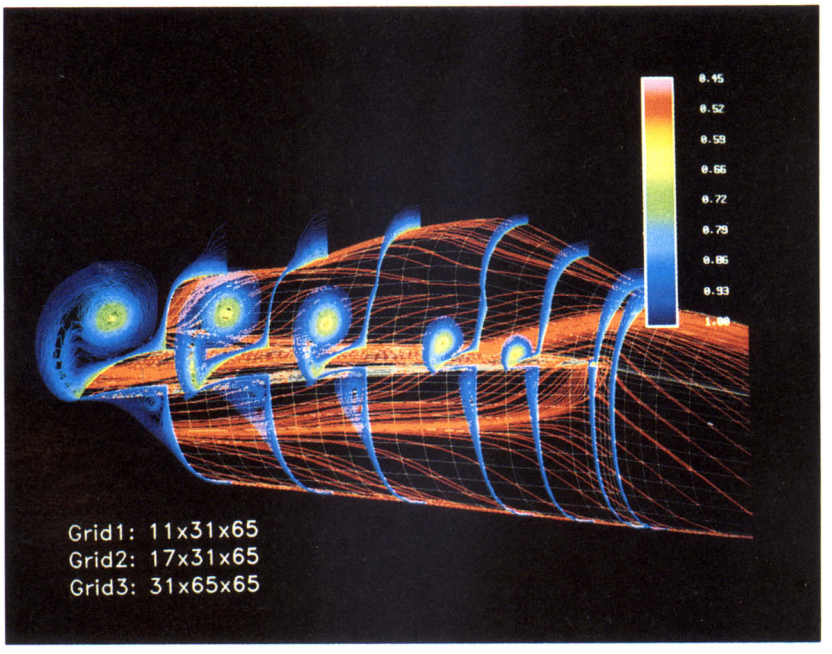

b) Turbulent

Fig. 4 Total pressure contours with surface flow pattern – LEX-body detail: $M_\infty = 0.6$, $R_{\bar{c}} = 0.8 \times 10^6$, $\alpha = 20$ deg.

in the open literature[1,3,6] as they have evolved. The flow is presumed to be governed by the unsteady Reynolds-averaged Navier-Stokes equations that are written in a body-fitted coordinate system. They are written in a usual conservation-law form as

$$\hat{Q}_{,t} + (\hat{F} - \hat{F}_v)_{,\xi} + (\hat{G} - \hat{G}_v)_{,\eta} + (\hat{H} - \hat{H}_v)_{,\zeta} = 0$$

Here, the subscripts with a comma denote partial differentiation, the subscript v identifies the viscous terms, and the superscript $\hat{}$ indicates scaling with respect to the Jacobian of the coordinate transformation. Details for these terms are included in Ref. 15. With the ideal gas assumption, the pressure and total enthalpy can be expressed as

$$p = (\gamma - 1)(E_0 - 1/2\,\rho q^2); \quad h_0 = [\gamma/(\gamma - 1)](p/\rho) + 1/2\,q^2$$

For the present study, the thin layer approximation to the governing equations is invoked (ie., $\hat{F}_v = \hat{G}_v = 0$) thus accounting for viscous flux terms only in the ζ direction (normal to the body).

Turbulence effects are accounted for through the notion of an eddy viscosity and eddy conductivity:

$$\mu = \mu_l + \mu_t = \mu_l(1 + \mu_t/\mu_l)$$

$$k = k_l + k_t = k_l(1 + k_t/k_l) = (c_p\mu_l/Pr_l)[1 + (\mu_t Pr_l/\mu_l Pr_t)]$$

where the subscripts l and t denote laminar and turbulent, respectively. The algebraic turbulence model developed by Baldwin and Lomax[16] is used to evaluate appropriate turbulence quantities. For separated flow regions, the notions of

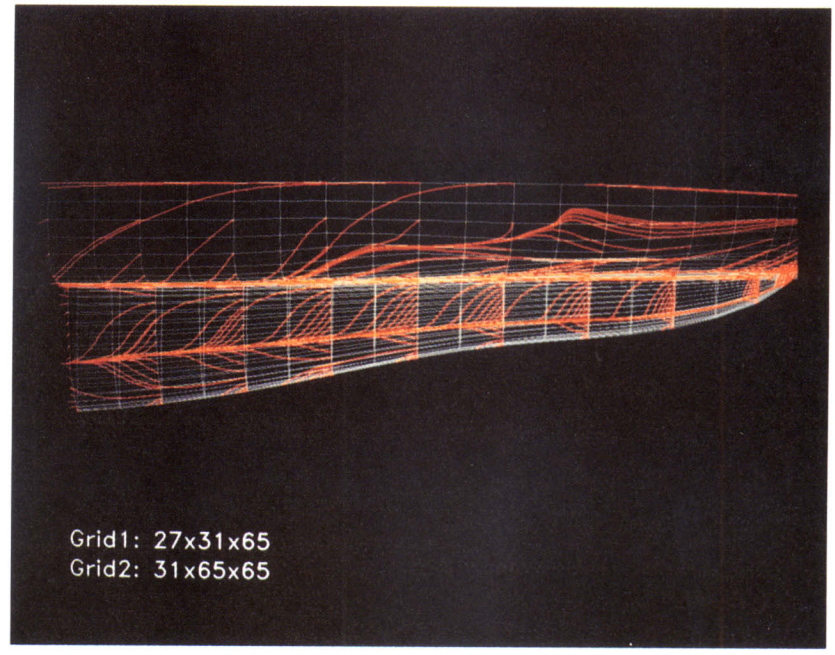

a) Laminar

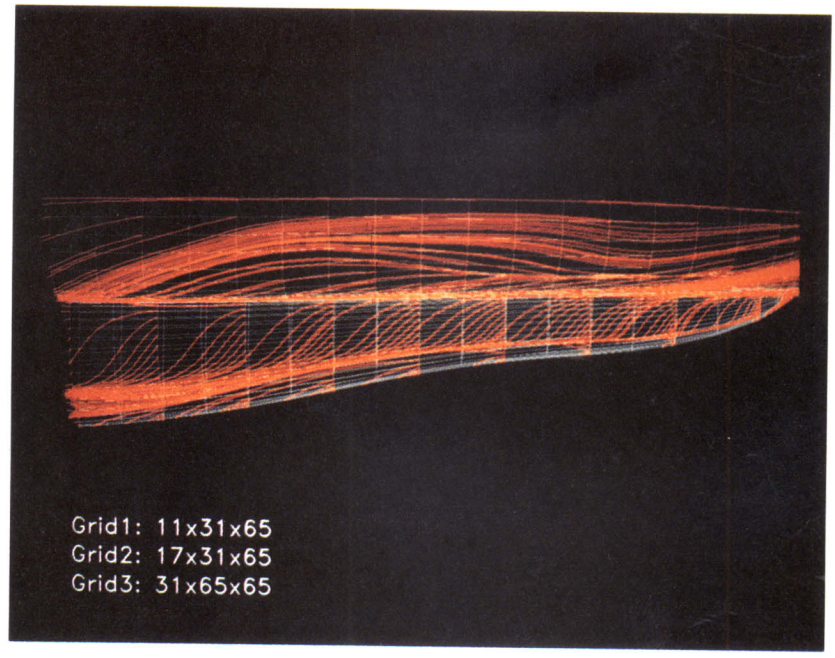

b) Turbulent

Fig. 5 LEX upper surface flow pattern: $M_\infty = 0.6$, $R_{\hat{c}} = 0.8 \times 10^6$, $\alpha = 20$ deg.

Degani and Schiff[17] are drawn upon to determine proper turbulence length scales.

Computational Method

Discretization of the governing equations results in a consistent approximation to the conservation laws in integral form

$$\frac{\partial}{\partial t}\iiint \hat{Q}\, dV + \iint \hat{f}\cdot\hat{n}\, dS = 0$$

where the time rate of change of the state vector $\hat{Q}$ within a cell is balanced by the net flux $\hat{f}$ across the cell surface. Flux quantities are represented using the upwind-biased, flux-difference-splitting approach of Roe[18] with third-order accuracy. Salient aspects of this formulation are included in Appendix 2 of Ref. 15, and additional details have been given by Vatsa et al.[6] Solutions are advanced in time with a spatially split, three-factor approximate factorization method in diagonalized form.

Interface quantities between longitudinal blocks are determined in a conservative second-order accurate manner. At the interface between the two blocks, the conserved variables are interpolated across the overlapping mesh area using a technique introduced by Ramshaw.[19] The conservation of mass, momentum, and energy are maintained across the interface boundary by redistributing the fluxes from one side onto the cell faces of the opposite side. A detailed discussion of the patching algorithm is given by Thomas et al.[20]

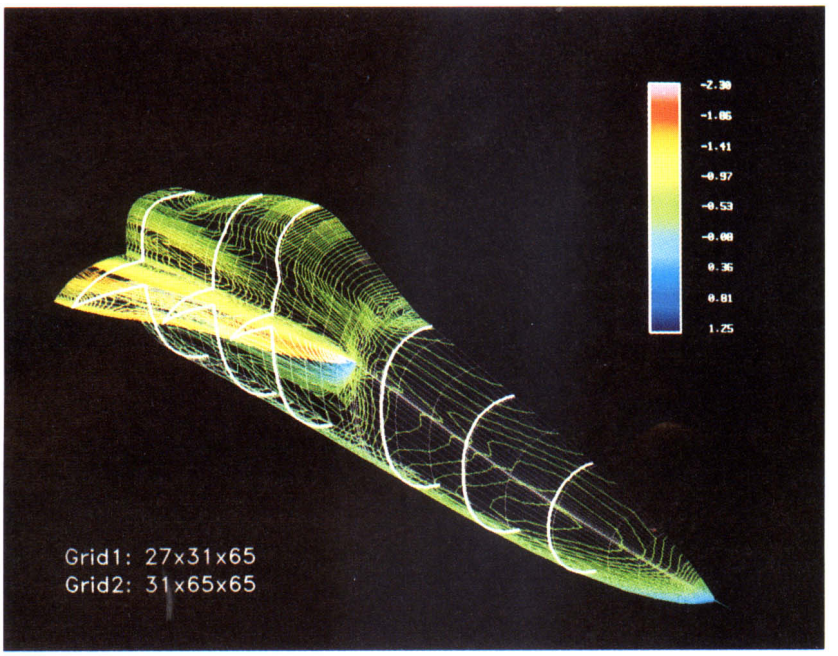

a) Laminar

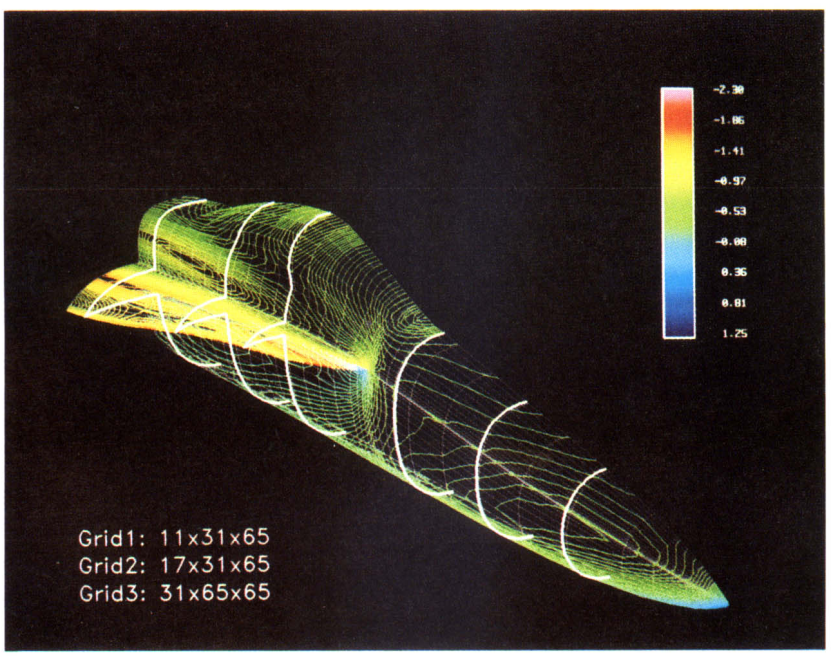

b) Turbulent

Fig. 6 Static surface pressure coefficient contours: $M_\infty = 0.6$, $R_{\bar{c}} = 0.8 \times 10^6$, $\alpha = 20$ deg.

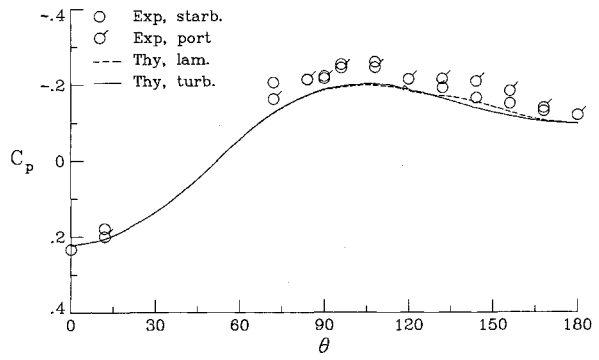

a) Station 1, $x/\bar{c} = 0.334$

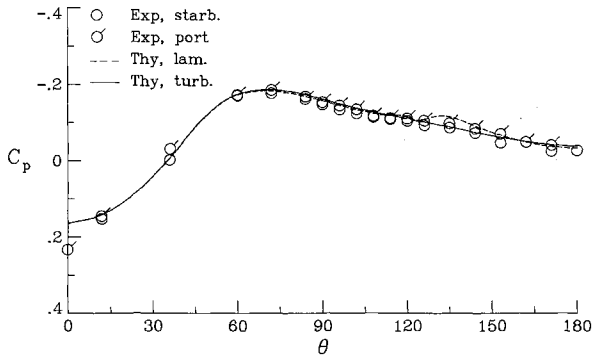

b) Station 2, $x/\bar{c} = 0.587$

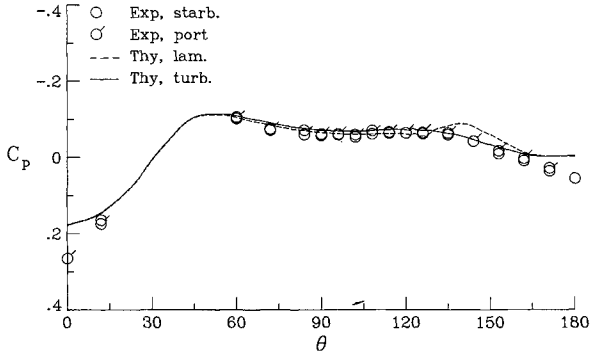

c) Station 3, $x/\bar{c} = 0.891$

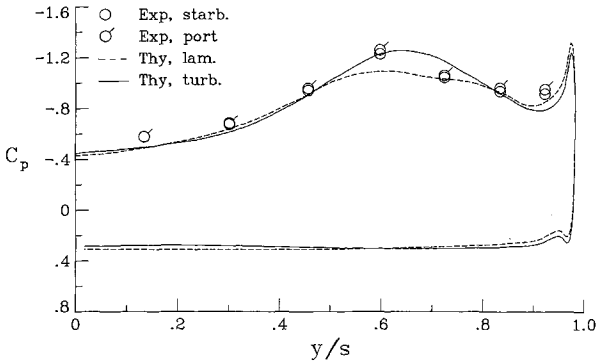

d) Station 4, $x/\bar{c} = 1.390$

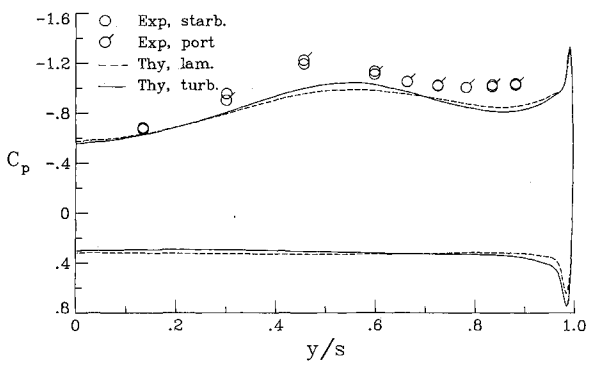

e) Station 5, $x/\bar{c} = 1.701$

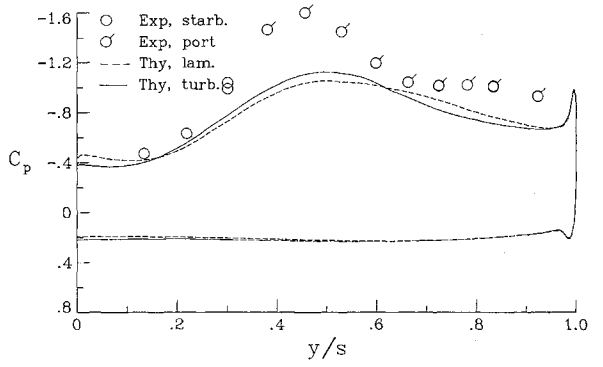

f) Station 6, $x/\bar{c} = 2.143$

Fig. 7 Correlation between theory and experiment – surface C_p: $M_\infty = 0.6$, $R_{\bar{c}} = 0.8 \times 10^6$, $\alpha = 20$ deg.

Surface Definition and Grid

The surface definition for the F/A-18 forebody-LEX geometry is obtained from a detailed computer aided design (CAD) description of the 6% scale model tested by Erickson.[13] The configuration is modeled from the nose longitudinally back to $x/\bar{c} = 2.337$, a station slightly ahead of the LEX-wing juncture ($x/\bar{c} = 2.482$) at which point the LEX leading edge has already achieved 90 deg of sweep. A downstream extension of the surface is then obtained by repeating the cross-sectional geometry from this station as described in the following paragraphs.

The grid is divided into two longitudinal blocks that interface along a plane x = const at the LEX apex station, Fig. 1. The forward block extends upstream of the nose by approximately 1.5 $\bar{c}$ and the aft block extends downstream of the LEX-wing station by approximately 1.5 $\bar{c}$; both blocks extend radially from the model centerline by approximately 2.4 $\bar{c}$. (For the downstream extension, the model cross section is held constant.) The reference length $\bar{c}$ is comparable to the longitudinal extent of the forebody and three-quarters of the longitudinal extent of the LEX-body juncture.

The three-dimensional grid for each block is constructed from two-dimensional O-type crossflow grids that are longitudinally stacked, constituting an H-O topology. The crossflow grids are generated using established transfinite interpolation techniques[21,22] with a method applicable to slender shapes.[23] Both blocks have 65 points in the radial direction; the upstream block has 31 circumferential points, whereas the downstream block has an additional 34 points in the circumferential direction to represent the LEX. With the blocked approach, the LEX apex is represented as a singular point while the body representation is continuous through this station. Longitudinally, the grid is clustered near the nose and LEX-apex regions with 17 stations on the forebody and 22 stations on the LEX body. The grid is completed with 10 stations extending upstream from the nose and 9 stations extending downstream from the station $x/\bar{c} = 2.337$; both extensions incorporate longitudinal stretching to provide resolution near the configura-

tion. The F/A-18 forebody-LEX surface geometry is represented with a total of 1957 points, and the entire baseline grid consists of approximately 185,000 points. For the turbulent flow computation, the upstream extension of the grid ahead of the nose apex is treated as a separate block without making any alterations to the grid itself.

The baseline grid is generated with sufficient normal clustering near the surface to adequately resolve the laminar sublayer for the turbulent boundary layer flow at the subject wind-tunnel freestream conditions ($M_\infty = 0.6$, $R_{\bar{c}} = 0.8 \times 10^6$, and $\alpha = 20$ deg). This grid produced an average normal cell-center size next to the wall of approximately $10^{-4}\bar{c}$, which corresponds to $y^+ \approx 2$ for the turbulent computations; a laminar sublayer generally extends out to $y^+ \approx 8.5$. The same grid is used for the laminar computations as well. Figure 2a illustrates the nearfield grid structure about a typical F/A-18 LEX-body cross section. This figure illustrates the challenge that is associated with generating a single O-type grid around such a complex cross section with various break points in the surface geometry. Additional details of the grid resolution in the LEX-body juncture is shown in Fig. 2b.

At the subject flight freestream conditions ($M_\infty = 0.34$, $R_{\bar{c}} = 13.5 \times 10^6$, and $\alpha = 19$ deg), the baseline grid produced $y^+ \approx 8$. Although an average y^+ slightly less than 10 has been reported[10] to provide adequate viscous resolution, a grid sensitivity investigation was conducted to provide solutions at flight conditions with comparable viscous resolution to those already achieved at wind-tunnel conditions. The baseline grid was modified to have twice the number of points in the normal direction with increased clustering such that approximately 4.5 fine grid cells were packed in the first cell of the baseline grid. The longitudinal and circumferential grid distributions were

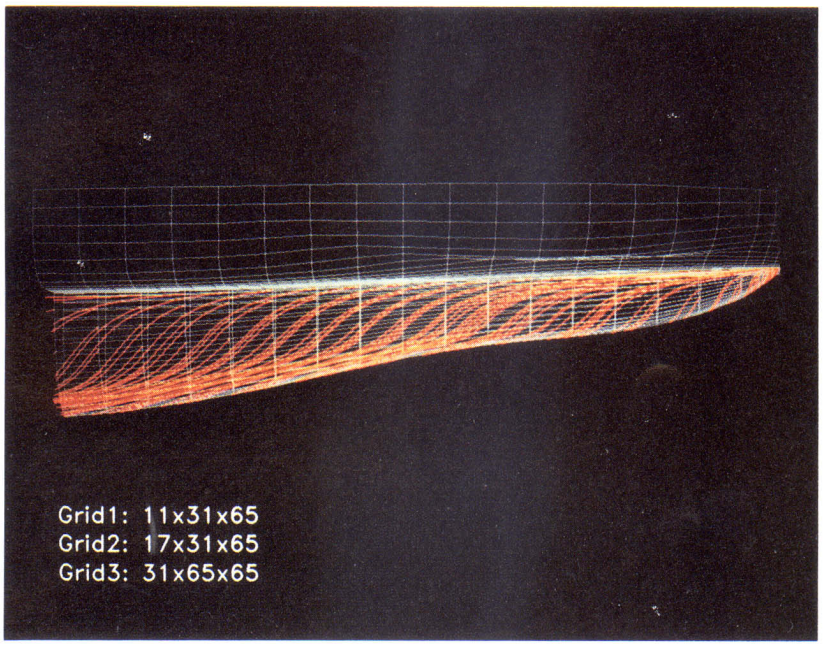

a) Baseline grid

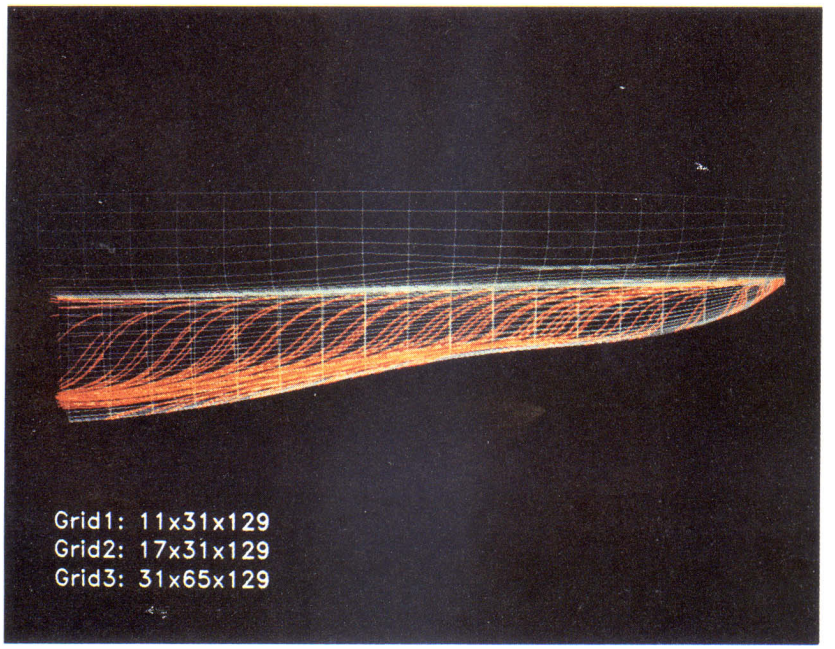

b) Refined grid

Fig. 8 LEX upper surface flow pattern: $M_\infty = 0.34$, $R_{\bar{c}} = 13.5 \times 10^6$, $\alpha = 19$ deg.

not altered. The resultant fine grid consists of approximately 370,000 points and yields $y^+ \approx 3$ for the turbulent computations at flight conditions.

Results and Discussion

All computations were performed on the NAS Cray 2, located at NASA Ames Research Center. On this machine, the algorithm requires approximately 22 μs per grid point per cycle on a single processor. Converged results were obtained in nominally 2200 cycles requiring about 2.5 h of computer time for the baseline grid. This number of cycles was sufficient to reduce the residuals by two to three orders of magnitude and limit the oscillations in C_L to $\approx \pm 0.14\%$ of the mean value for the last ≈ 300 cycles. The computations were performed without the use of mesh sequencing or multigrid iteration.

Results are presented for the subject wind-tunnel and flight-test conditions. All comparisons of computed results (e.g., laminar vs turbulent, baseline vs refined grid, etc.) within a figure are presented from an identical vantage point. The grid dimensions for each particular computation are given in each figure (the term "Grid" in these figures refers to the block number). The magnitudes associated with contour quantities are displayed with a color bar.

Wind-Tunnel Computations

The computed total pressure contours and surface streamline patterns are shown in Figs. 3 for both laminar as well as turbulent flow calculations. These solutions are obtained at $M_\infty = 0.6$, $R_{\bar{c}} = 0.8 \times 10^6$, and $\alpha = 20$ deg. The crossflow total pressure contours for the laminar computations (Fig. 3a) clearly show

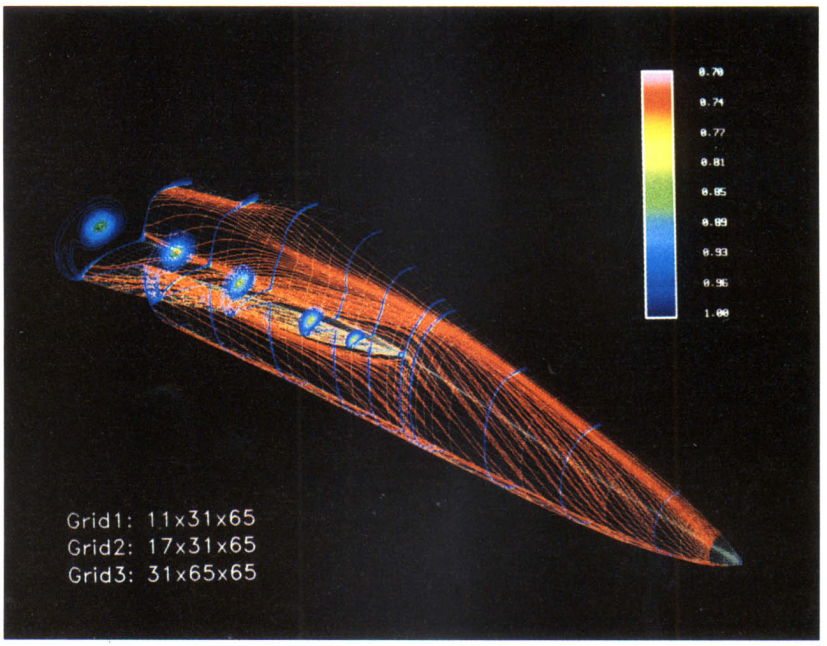

a) Overall view

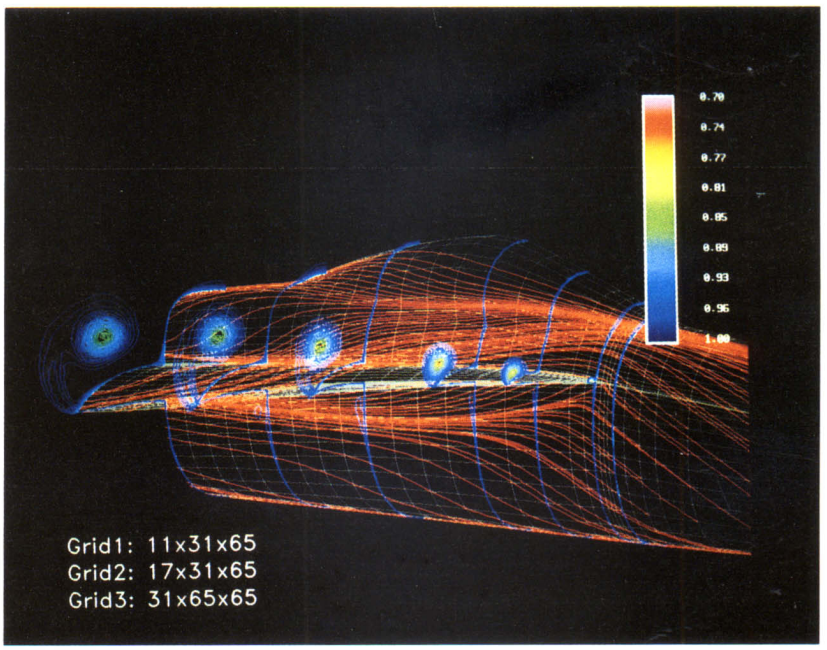

b) LEX-body detail

Fig. 9 Total pressure contours with surface flow pattern: $M_\infty = 0.34$, $R_{\bar{c}} = 13.5 \times 10^6$, $\alpha = 19$ deg.

the LEX primary and the secondary vortex systems. In addition, the same crossflow contours show an appreciable body type separation under the LEX, which will be discussed later in detail. Furthermore, there exists a clear primary separation line (as indicated by the converging surface streamlines) on the forebody along with a secondary separation line on the leeward side of the aft forebody. These are fairly flat bubble-type separations that, in general, occur on the order of a boundary-layer thickness. The primary and the secondary separation lines merge and wrap around the LEX apex with a subsequent entrainment into the juncture between the LEX upper surface and the body. The turbulent flow computations demonstrate a drastically different flow structure as shown in Fig. 3b. For example, it appears that the primary and the secondary separation lines on the forebody are completely eliminated in the turbulent case. Additional differences are discussed subsequently.

A closeup view of the LEX-body flow structure is shown in Figs. 4 for both laminar and turbulent flow. These results show the very complex flow that exists under the LEX, especially for the laminar flow solution (Fig. 4a). It appears that, for this result, there is a bubble-type separation under the LEX apex, similar to what occurred on the forebody, with closely coupled primary and secondary separation lines. Further downstream a larger vortex-like separation is evident with a more distinguishable primary (closer to windward plane of symmetry) and secondary (close to LEX-body juncture) separation lines. However, the transition of the primary separation line between the front and aft region does not appear to have been grid resolved. Once again there are significant differences between laminar and turbulent computations as shown in Fig. 4b. The body separation under the LEX is changed considerably by occurring closer to the LEX lower surface and practically filling up the entire corner region. The separation pattern for the turbulent case is much simpler than the corresponding pattern for the laminar case.

Figure 4 also provide a close view of the surface flow in the vicinity of the longitudinal grid-patching station (i.e., the LEX

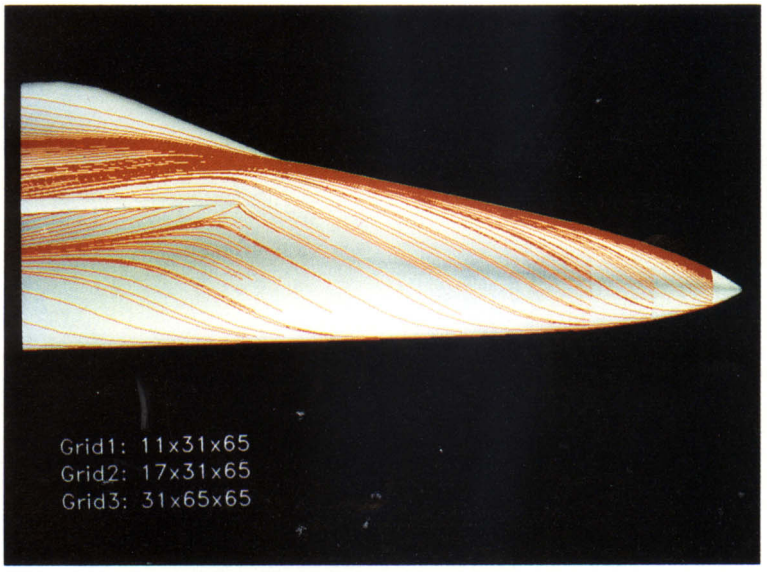

a) Computational results

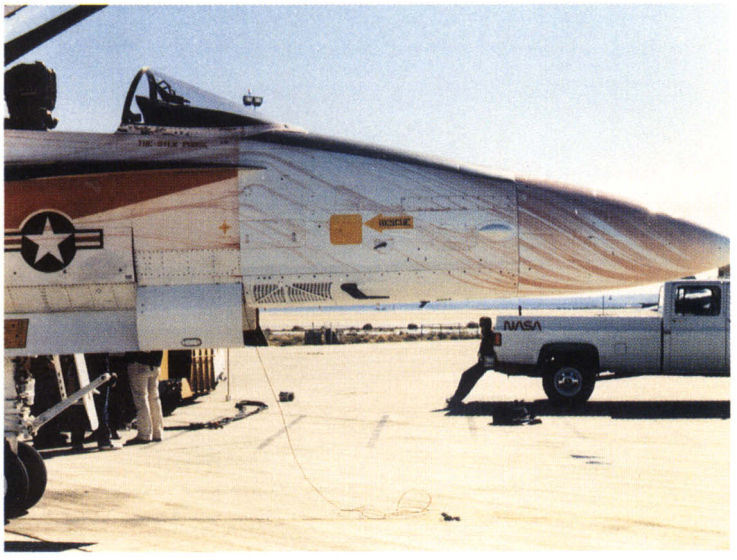

b) Flight test

Fig. 10 Comparison of turbulent surface streamlines with flight test – side view: $M_\infty = 0.6$, $R_{\bar{c}} = 0.8 \times 10^6$, $\alpha = 20$ deg.

apex station). Note that the flow properties are very smooth across this interfacing patch between the two blocks of grid.

The LEX upper surface flow pattern computed at the wind-tunnel flow conditions for both laminar and turbulent flow are shown in Fig. 5. The laminar computation (Fig. 5a) clearly shows the secondary separation line with the subsequent reattachment line (indicated by the diverging surface streamlines) between the secondary separation line and the leading edge. As expected, the turbulent flow computation (Fig. 5b) shows the outboard movement of the secondary separation line.

Contours of the static surface pressure coefficient are shown in Fig. 6 for both laminar and turbulent flow computations. The results show a compression region around the apex of the LEX as well as the footprint of low pressure associated with the LEX primary and secondary vortices on the LEX upper surface. Although these surface contours of the laminar and turbulent solutions look very similar, a more detailed assessment indicates significant differences, as will be discussed subsequently in conjunction with experimental wind-tunnel data. The experimental stations are highlighted in white and are located at $x/\bar{c} = 0.334$, 0.587, 0.891, 1.390, 1.701, and 2.143. For reference, the LEX apex is located at $x/\bar{c} = 1.006$ and the LEX-wing juncture at $x/\bar{c} = 2.482$.

The comparison of the computed surface pressure coefficients for both laminar and turbulent flow is shown in Fig. 7 at the six different stations. The experimental data are also shown for both the starboard and port sides of the model to assess flow symmetry. Figures 7a–c show the variation of the surface pressure coefficients as a function of azimuthal angle θ on the forebody. The windward and leeward sides of the forebody correspond to $\theta = 0$ and 180 deg, respectively. Both laminar and turbulent solutions slightly underpredict the pressure peak at station 1 as shown in Fig. 7a. This underprediction of the pressure peak could well be attributed to the inability of the H-O grid topology to resolve the flow near forebody nose. This figure also indicates the differences between the laminar and turbulent solutions that occur in the range 130 deg $\leq \theta \leq$ 165 deg. This difference is due to the separated zones on the forebody that occur for laminar flow. Figures 7b and 7c show a very good correlation between the computational results and the experimental data, particularly the turbulent flow solution. The differences between theory and experiment shown in Fig. 7c near $\theta = 0$ and 180 deg are believed to be associated with circumferential grid resolution.

The computed surface pressure coefficients on the LEX are shown in Figs. 7d–f along with the experimental data as a

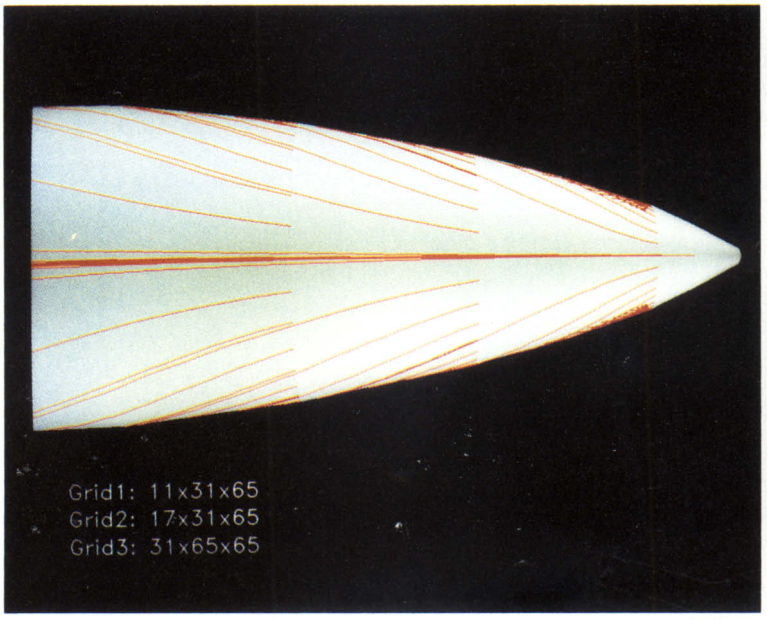

a) Computational results

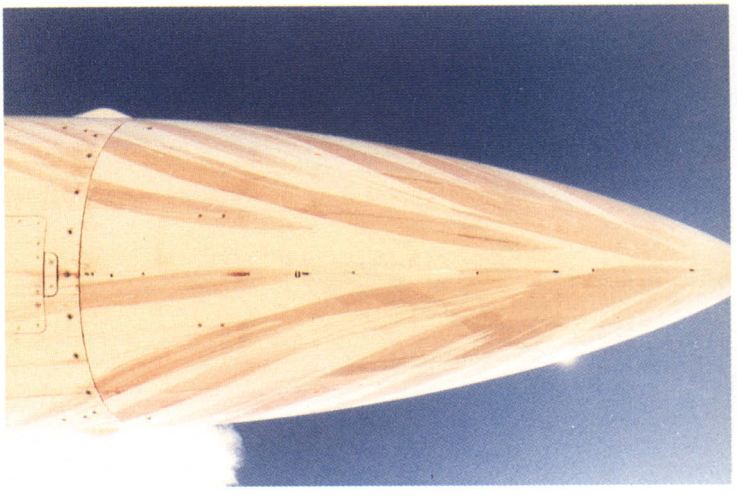

b) Flight test

Fig. 11 Comparison of turbulent surface streamlines with flight test – bottom view: $M_\infty = 0.6$, $R_{\bar{c}} = 0.8 \times 10^6$, $\alpha = 20$ deg.

function of LEX exposed semispan, y/s. In this way, $y/s = 0$ corresponds to the LEX-body juncture and $y/s = 1$ corresponds to the LEX leading edge. Figure 7d reveals a good agreement between the experimental data and the turbulent flow computation. This figure also shows that the laminar flow underpredicts the low pressure peak that is associated with the primary vortex system. This difference between the laminar and turbulent solutions is not as evident on the color surface pressure contours shown earlier in Fig. 6. The correlation between theory and experiment begins to degrade at station 5 (Fig. 7e) and continues to do so at station 6 (Fig. 7f). It is believed that this difference is primarily associated with wing-induced upwash effects present in the experimental data. The test was conducted with a complete F/A-18 configuration, including flow-through inlets, whereas the computations only modeled the forebody-LEX portion of the configuration. The wing-induced effects would be strongest near the aft portion of the LEX and, in general, would cause more negative suction pressures by strengthening the LEX vortex. Inlet-induced effects are a secondary source for this discrepancy. Nonetheless, it is noteworthy that the forebody pressures as well as the pressures on the forward portion of the LEX can be accurately predicted with the turbulent computations on the isolated forebody-LEX geometry.

The correlation between theory and experiment is further assessed in Ref. 15 by examining the experimental sensitivity of the surface pressure to changes in angle of attack of ± 2.5 deg as well as changes in freestream Mach number from 0.4 to 0.8. The difference between theory and experiment are shown to be, in general, significantly less than the incremental effects of α and M_∞ in the experiment.

Flight-Test Computations

The flight-test solutions are obtained at $M_\infty = 0.34$, $R_{\bar{c}} = 13.5 \times 10^6$, and $\alpha = 19$ deg. Because of the high Reynolds number associated with flight, grid sensitivity effects were assessed. Various flow parameters (e.g., Mach contours, density contours, surface flow patterns, surface pressure contours, etc.) were contrasted between the solutions obtained with either the baseline or the refined grid. No major differences between these solutions were found. Typical results that contrast the baseline and refined grid solutions are presented in Figs. 8 for the LEX upper surface flow pattern. Additional discussion on the effects of grid refinement on the computed results have been reported by Ghaffari et al.[15] It was concluded from this study that the baseline grid provided credible solutions that could be used for the subsequent correlations with the flight-test results.

The total pressure contours at various crossflow stations as well as the surface flow pattern computed at flight condition are shown in Figs. 9. Figure 9a shows an overall view of the flow, whereas Fig. 9b illustrates the LEX-body flow details. The forebody surface flow pattern qualitatively resembles the turbulent solution obtained at wind-tunnel flow conditions (c.f., Fig. 3b) in that the flow appears to remain attached. The LEX-body flow exhibits greater differences between flight (Fig. 9b) and wind-tunnel (Fig. 4b) conditions principally with respect to the body separation under the LEX. This separated zone is smaller at the flight conditions than was observed in the wind-tunnel computations.

A side view of the computed surface flow streamlines on the forebody at flight condition is shown in Fig. 10a. This figure also shows part of the LEX geometry. The surface flow pattern obtained in flight is shown in Fig. 10b from a similar vantage point. The body separation line under the LEX is well predicted by the turbulent computations. Furthermore, the overall surface flow pattern around the forebody agrees well, qualitatively, with the flight-test results. Similarly, Figs. 11 show a correlation between the computed surface streamlines and the flight-test results on the windward side (of the front part) of the forebody. The correlation between these results is also quite good.

Concluding Remarks

Three-dimensional viscous flow computations for the F/A-18 forebody-LEX are presented for both wind-tunnel as well as flight conditions. At wind-tunnel condition, significant difference between laminar and turbulent solutions are revealed, particularly on the surface flow pattern. Good agreement between the computed surface pressure coefficient and the experimental data is also disclosed. The turbulent computations provided a better correlation with the data. At flight conditions, the grid sensitivity study indicated that the baseline grid clustering with only 185,000 grid points was sufficient to resolve the viscous laminar sublayer for the turbulent computations. Qualitatively, the computed surface flow pattern is in good agreement with the flight-test results. Finally, from a practical point of view, the converged results presented for the baseline grid were achieved with a nominal 2200 cycles requiring about 2.5 h of Cray-2 computer time.

Acknowledgments

NASA Langley Research Center sponsored the work of the first and fourth authors under NASA Contract NAS1-17919. The authors wish to thank Gary Warren of NASA Langley Research Center for providing the original F/A-18 forebody-LEX surface definition. The authors also wish to thank Dave Fisher of the NASA Dryden Flight Research Facility for providing surface flow visualization photographs of the NASA F/A-18 HARV along with supporting flight data.

References

[1]Thomas, J. L., and Newsome, R. W., "Navier-Stokes Computations of Lee-Side Flows over Delta Wings," AIAA Paper 86-1049, 1986.

[2]Vatsa, V. N., "Accurate Solutions for Transonic Viscous Flow over Finite Wings," AIAA Paper 86-1052, 1986.

[3]Thomas, J. L., Taylor, S. L., and Anderson, W. K., "Navier-Stokes Computations of Vortical Flows over Low Aspect Ratio Wings," AIAA Paper 87-0207, 1987.

[4]Newsome, R. W., and Adams, M. S., "Numerical Simulation of Vortical-Flow over an Elliptical-Body Missile at High Angles of Attack," AIAA Paper 86-0559, 1986.

[5]Ying, S. X., Steger, J. L., Schiff, L. B., and Bagdanoff, D., "Numerical Simulation of Unsteady, Viscous, High Angle of Attack Flows Using a Partially Flux-Split Algorithm," AIAA Paper 86-2179, 1986.

[6]Vatsa, V. N., Thomas, J. L., and Wedan, B. W., "Navier-Stokes Computations of Prolate Spheroids at Angle of Attack," AIAA Paper 87-2627, 1987.

[7]Walters, R. W., Reu, T., McGrory, W. D., Thomas, J. L., and Richardson, P. F., "A Longitudinally-Patched Grid Approach with Applications to High Speed Flows," AIAA Paper 88-0715, 1988.

[8]Eriksson, L.-E., Smith, R. E., Wiese, M. R., and Farr, N., "Grid Generation and Invisid Flow Computation about Cranked-Winged Airplane Geometry," AIAA Paper 87-1125, 1987.

[9]Szema, K. Y., Chakravarthy, S. R., and Bihari, B. L., "F-14 Flow Field Simulation," AIAA Paper 89-0642.

[10]Flores, J., and Chaderjian, N. M., "The Numerical Simulation of Transonic Separated Flow About the Complete F- 16A," AIAA Paper 88-2506, 1988.

[11]Deese, J. E., and Agarwal, R. K., "Navier-Stokes Calculations of Transonic Viscous Flow About Wing/Body Configurations," *Journal of Aircraft*, Vol. 25, No. 12, 1988, pp. 1106–1112.

[12]Buning, P. G., Chiu, I. T., Obayashi, S., Rizk, Y. M., and Steger, J. L., "Numerical Simulation of the Integrated Space Shuttle Vehicle in Ascent," AIAA Paper 88-4359, 1988.

[13]Erickson, G. E., Hall, R. M., Banks, D. W., Delfrate, J. H., Schreiner, J. A., Hanley, R. S., Pulley, C. N., "Experimental Investigation of the F/A-18 Vortex Flows at Subsonic Through Transonic Speeds," AIAA Paper 89-2222, 1989.

[14]Fisher, D. F., Richwine, D. M.,and Banks, D. W., "Surface Flow Visualization of Separated Flows on the Forebody of an F-18 Aircraft and Wind-Tunnel Model," NASA TM-100436, 1988.

[15]Ghaffari, F., Luckring, J. M., Thomas, J. L., and Bates B. L., "Navier-Stokes Solutions About the F/A-18 Forebody-LEX Configuration," AIAA Paper 89-0338, Jan. 1989.

[16]Baldwin, B. S., and Lomax, H., "Thin Layer Approximation and Algebraic Model for Separated Turbulent Flows," AIAA Paper 78-257, 1978.

[17]Degani, D., and Schiff, L. B., "Computation of Supersonic Viscous Flows Around Pointed Bodies at Large Incidence," AIAA Paper 83-0034, 1983.

[18]Roe, P. L., "Characteristic Based Schemes for the Euler Equations," *Annual Review of Fluid Mechanics*, 1986, pp. 337–365.

[19]Ramshaw, J. D., "Conservative Rezoning Algorithms for Generalized Two-Dimensional Meshes," *Journal of Computational Physics*, Vol. 59, 1985, pp. 193–199.

[20]Thomas, J. L., Walters, R. W., Reu, T., Ghaffari, F., Weston, R. P., and Luckring, J. M., "A Patched Grid Algorithm for Complex Configurations Directed Towards the F-18 Aircraft," AIAA Paper 89-0121, 1989.

[21]Eriksson, L. E., "Practical Three-Dimensional Mesh Generation Using Transfinite Interpolation," *Journal of Fluid Mechanics,* Vol. 148, 1984, pp. 45–78.

[22]Smith, R. E., *Algebraic Grid Generation. Numerical Grid Generation*, Elsevier, New York, 1982, pp. 137–168.

[23]Richardson, P. F., and Morrison, J. H., "Displacement Surface Calculations for a Hypersonic Aircraft," AIAA Paper 87- 1190, 1987.

Color reproduction courtesy of NASA Langley Research Center